

# Overview of nucleon structure studies <sup>★</sup>

Marc Vanderhaeghen

*Department of Physics, College of William and Mary, Williamsburg, Virginia 23187, USA  
Thomas Jefferson National Accelerator Facility, Newport News, VA 23606, USA*

---

## Abstract

A brief overview of the recent activity in the measurement of the elastic electromagnetic proton and neutron form factors is presented. It is discussed how the quality of the data has been greatly improved by performing double polarization experiments, and the role of two-photon exchange processes will be highlighted. The spatial information on the quark charge distributions in the nucleon resulting from the form factors measurements will be discussed, as well as the steady rate of improvements made in the lattice QCD calculations. It is discussed how generalized parton distributions have emerged as a unifying theme in hadron physics linking the spatial densities extracted from form factors with the quark momentum distribution information residing in quark structure functions. The recent progress in the electromagnetic excitation of the  $\Delta(1232)$  resonance will also briefly be discussed.

*Key words:* nucleon electromagnetic form factors, generalized parton distributions, nucleon excitation spectrum

*PACS:* 13.40.Gp, 14.20.Dh, 13.60.Fz, 14.20.Gk

---

## 1. Nucleon electromagnetic form factors

Electromagnetic form factors (FFs) of the nucleon are the standard source of information on the nucleon structure and as such have been studied extensively; for recent reviews see *e.g.* Refs. [1,2,3]. The most recent generation of electron accelerators, which combine high current with high polarization electron beams, at MIT-Bates, the Mainz Microtron (MAMI), and the Continuous Electron Beam Accelerator Facility (CEBAF) of the Jefferson Lab (JLab), have made it possible to investigate the internal structure

---

<sup>★</sup> This work is supported in part by DOE grant DE-FG02-04ER41302 and contract DE-AC05-06OR23177 under which Jefferson Science Associates operates the Jefferson Lab.

*Email address:* marcvdh@jlab.org (Marc Vanderhaeghen).

of the nucleon with unprecedented precision. In particular, the new generation of polarization experiments that make use of the target- and recoil-polarization techniques have allowed to chart the proton and neutron electromagnetic (e.m.) FFs very precisely.

The status of proton electric ( $G_{Ep}$ ) and magnetic ( $G_{Mp}$ ) FF measurements is shown in Fig. 1 (for more details and references, see [3]). The proton magnetic FF has been measured up to a momentum transfer  $Q^2$  of around 30 GeV<sup>2</sup>. The deviation of the proton magnetic FF from the standard dipole form  $G_D = 1/(1 + Q^2/0.71)^2$  has been measured precisely, showing a dip structure at low momentum transfers (around  $Q^2 \simeq 0.25$  GeV<sup>2</sup>) and a scaling behavior at very large values of  $Q^2$ . The recent and unexpected results from JLab of using the polarization transfer technique to measure the proton electric over magnetic FF ratio,  $G_{Ep}/G_{Mp}$  [4,5,6], has been the revelation that the FFs obtained using the polarization and Rosenbluth cross section separation methods, were incompatible with each other, starting around  $Q^2 = 3$  GeV<sup>2</sup> (see right panel on Fig. 1). The FFs obtained from cross section data had suggested that  $G_{Ep} \sim G_{Mp}/\mu_p$ , where  $\mu_p$  is the proton magnetic moment; the results obtained from recoil polarization data clearly show that the ratio  $G_{Ep}/G_{Mp}$  decreases linearly with increasing  $Q^2$ . The recoil polarization measurement for this ratio has been performed up to  $Q^2 = 5.6$  GeV<sup>2</sup>, and a new JLab experiment is extending this measurement (at the time of writing) up to  $Q^2 \simeq 8.5$  GeV<sup>2</sup>. The numerous attempts to explain the difference between both experimental techniques in terms of radiative corrections which affect the results of the Rosenbluth separation method very significantly, but polarization results only minimally, have led to the previously neglected calculation of two hard photon exchange with both photons sharing the momentum transfer, as discussed below.

The use of the polarization technique has also resulted in a constant progress in the measurement of  $G_{En}$ , which is intrinsically more difficult to obtain because of the smallness of this FF, due to the overall zero charge of the neutron. Recent times have seen the maximum  $Q^2$  for which we have polarization FFs grow to 1.5 GeV<sup>2</sup>, with new data obtained and under analysis up to 3.4 GeV<sup>2</sup>, and several experiments planned or proposed to significantly higher  $Q^2$  values. Important progress has been made for  $G_{Mn}$  too, with new data with much improved error bars up to 4.8 GeV<sup>2</sup>, see Fig. 2.

When comparing the precision data for the nucleon e.m. FFs in Figs. 1 and 2, Friedrich and Walcher [10] made the striking observation that all four FFs display “bump structures” around  $Q^2 \simeq 0.25$  GeV<sup>2</sup>. They interpret this structure as a signature of the pion cloud. For a comparison with new data of the BLAST Coll. at low  $Q^2$  for both proton and neutron, see [9].

Given the large amount of precise data on FFs it is of interest to exhibit directly the spatial information which results from these data. When viewing the nucleon from a light front moving towards the nucleon, a model independent 2-dimensional mapping of the quark charge density in the nucleon can be achieved in the transverse plane (perpendicular to the direction of motion). Using only the empirical information on the nucleon e.m. FFs, these transverse charge densities have been extracted recently for an unpolarized nucleon [11], as well as for a transversely polarized nucleon [12].

In Fig. 3 these transverse charge densities are shown for proton and neutron, both for the unpolarized case and for a nucleon polarized along the  $x$ -axis (denoting the direction of the fast moving frame by the  $z$ -axis). One notices from Fig. 3 that polarizing the proton along the  $x$ -axis leads to an induced electric dipole field which corresponds with an electric dipole moment along the negative  $y$ -axis equal to the value of the anomalous magnetic

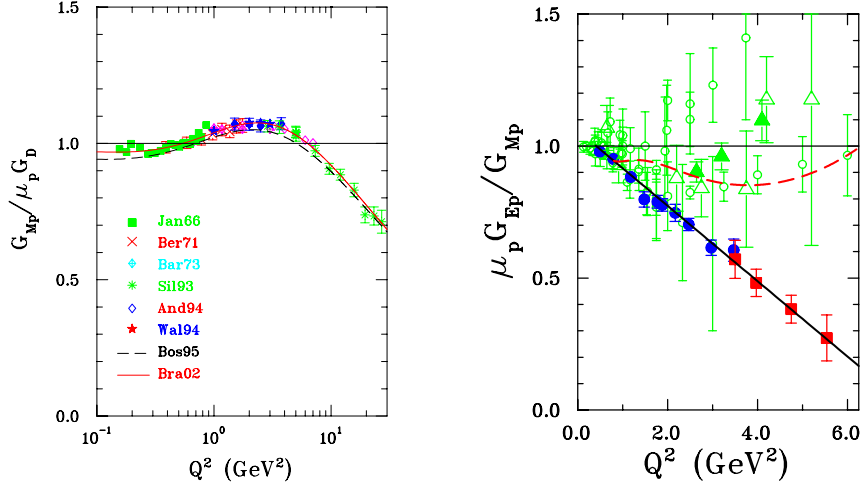


Fig. 1. Left panel : world data base for  $G_{Mp}$  obtained by the Rosenbluth method; the references can be found in [3]. Right panel : comparison of  $\mu_p G_{Ep}/G_{Mp}$  from the two JLab polarization data [5,6] (solid circles and squares), and Rosenbluth separation results (symbols as referred to in Ref. [3]). Dashed curve is a re-fit of Rosenbluth data [7]; solid curve is a fit to the JLab polarization data.

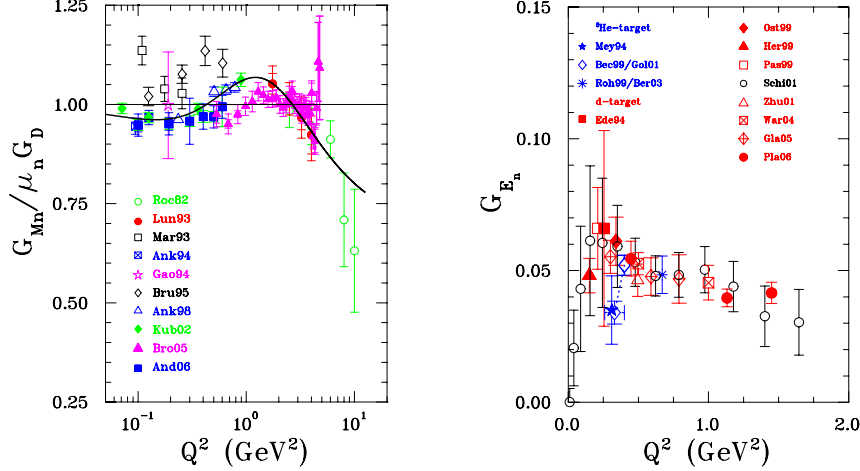


Fig. 2. Left panel : world data base for  $G_{Mn}$ , from cross section and polarization measurements. Shown as a solid curve is the polynomial fit by Kelly [8]. Right panel : world data for  $G_{En}$  from beam asymmetry with polarized  $D_2$ , and  $^3\text{He}$ , and recoil polarization with  $D_2$ . For references see [3].

moment, *i.e.*  $\kappa_N$  (in units  $e/2M_N$ ) as noticed in [13]. One sees that the corresponding neutron's transverse charge density gets displaced significantly due to the large (negative) value of the neutron anomalous magnetic moment,  $\kappa_n = -1.91$ , which yields an induced electric dipole moment along the positive  $y$ -axis.

To calculate nucleon e.m. FFs from first principles, lattice QCD simulations have seen an important progress in recent years. State-of-the-art lattice calculations for nucleon structure studies use lattice spacings  $a \lesssim 0.1$  fm and lattice sizes  $L \sim 3$  fm and reach pion mass values down to about 350 MeV. To connect those results with the physical world

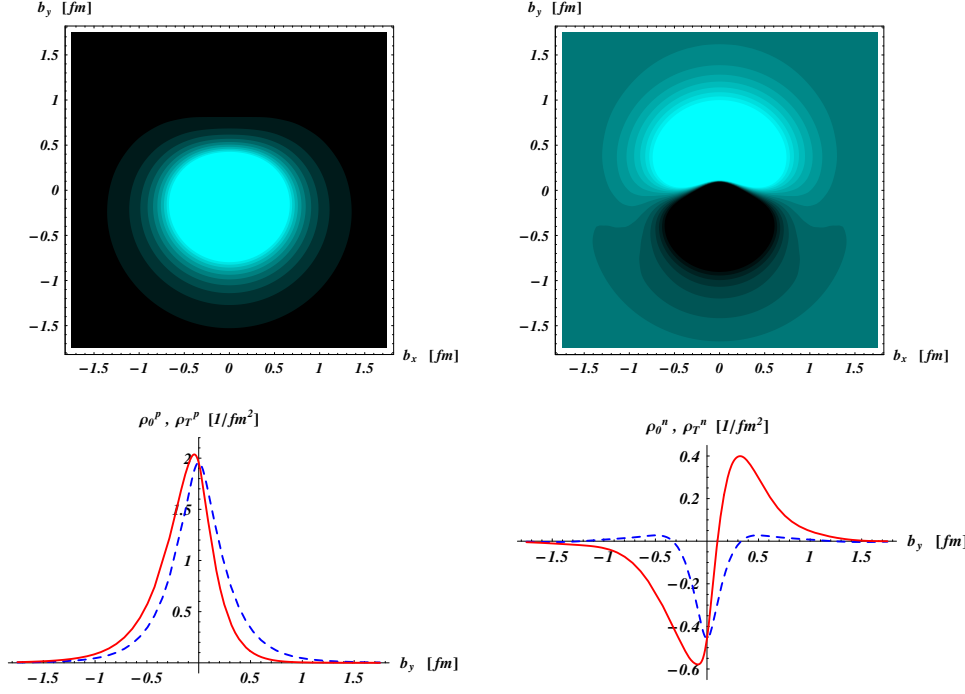


Fig. 3. Quark transverse charge densities in the *proton* (left panels) and *neutron* (right panels). The upper panel shows the density in the transverse plane for a nucleon polarized along the  $x$ -axis. The light (dark) regions correspond with largest (smallest) values of the density. The lower panel compares the density along the  $y$ -axis for an unpolarized nucleon (dashed curve), and for a nucleon polarized along the  $x$ -axis (solid curve). For the proton (neutron) e.m. FFs, the empirical parameterization of Arrington *et al.* [14] (Bradford *et al.* [15]) is used. Figure from [12].

requires an extrapolation down to the physical quark mass  $m_q$  (with  $m_q$  proportional to  $m_\pi^2$ ). It is only very recently that pion mass values below 350 MeV [16] have been reached. This continuous effort is important to eliminate one source of systematic error associated with the extrapolation to the light quark masses.

The lattice calculations for the (space-like) nucleon e.m. FFs require the evaluation of three-point functions, which involve two topologically different contributions. In the connected diagram contribution, the photon couples to one of the quarks connected to either the initial or final nucleon. The disconnected diagram, which involves a coupling to a  $q\bar{q}$  loop, requires a numerically more intensive calculation, is at present neglected in most lattice studies. When taking the difference between proton and neutron e.m. FFs, i.e. for the isovector combination, the disconnected contribution drops out. Therefore, the calculations in which the disconnected diagram is neglected are applicable only to the isovector e.m. FFs.

Fig. 4 shows the unquenched lattice QCD results from the LHPC Coll. for the nucleon e.m. FFs, performed for one lattice spacing of  $a \simeq 0.125$  fm, and for pion mass values in the range  $m_\pi = 360 - 775$  MeV. It is seen that this action yields a noticeable dependence on  $m_\pi$  for the Dirac isovector FF  $F_1^V$ . The  $Q^2$  dependence of  $F_1^V$  at the smallest  $m_\pi$  value

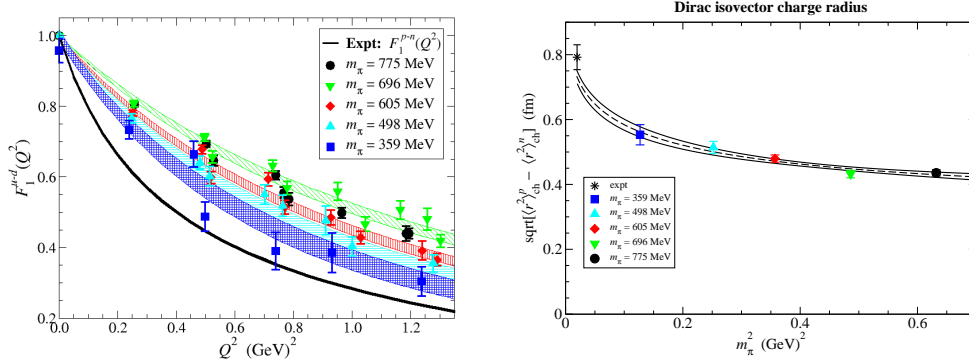


Fig. 4. Left panel : Lattice QCD results (from the LHPC Coll. [17]) for the nucleon isovector FF  $F_1^V$ . The unquenched results using a hybrid action of domain wall valence quarks and 2+1 flavor staggered sea quarks are shown for different values of  $m_\pi$  and are compared with experiment (solid curve, using the parameterization of [8]). Right panel : Chiral extrapolation of the nucleon isovector Dirac radius  $\langle r^2 \rangle_1^V$ . The unquenched results are from the LHPC Coll. [17]. The experimental value is shown by the star. The curves are fits using the chiral extrapolation formula Eq. (1).

of around 360 MeV is found to be in qualitative agreement with the data. Evidently, it will be very worthwhile to corroborate the results at the lowest pion masses and improve their statistics in future calculations. For lattice calculations of the isovector FFs using Wilson fermions, from the QCDSF Coll., see [16]; and for calculations using dynamical domain wall fermions, from the RBC and UKQCD Coll., see [18].

Present lattice calculations are possible for larger than physical quark masses, and therefore necessitate an extrapolation procedure in order to make contact with experiment. The extrapolation in  $m_q$  is not straightforward, because the non-analytic dependencies, such as  $\sqrt{m_q}$  and  $\ln m_q$ , become important as one approaches the small physical value of  $m_q$ . As an example, the Dirac charge radius,  $\langle r^2 \rangle_1^V$  varies as  $\ln m_\pi^2$  when approaching the chiral limit. To extend the range of validity in  $m_\pi$  of such a prediction, a one may try in this spirit a modification of the chiral perturbation theory formula as [19] :

$$\langle r^2 \rangle_1^V = a_0 - \frac{1 + 5g_A^2}{(4\pi f_\pi)^2} \ln \left( \frac{m_\pi^2}{m_\pi^2 + \Lambda^2} \right), \quad (1)$$

where  $\Lambda$  is a phenomenological cut-off which reflects the finite size of the nucleon, with  $a_0$  a low-energy constant. The other parameters in this expression are fixed and well known. Such a fit (using  $\Lambda \sim 500$  MeV) for the isovector Dirac radius is shown in Fig. 4 and compared with the most recent unquenched lattice results using the hybrid action (domain wall valence quarks on top of a 2+1 flavor staggered sea) of the LHPC Coll. One firstly sees, that these lattice results do show appreciable  $m_\pi^2$  variation over the pion mass range  $m_\pi = 360 - 775$  MeV and provide a first clear hint of the logarithmic  $m_\pi$  divergence. As the pion mass approaches the physical value, the calculated nucleon size increases and approaches the correct value.

At larger momentum transfers, the striking difference between the unpolarized (Rosenbluth) and polarization transfer measurements of the proton  $G_{Ep}/G_{Mp}$  FF ratio has triggered a renewed interest in the field of two-photon exchange in  $eN$  scattering experiments. Theoretical calculations both within a hadronic and partonic framework made it

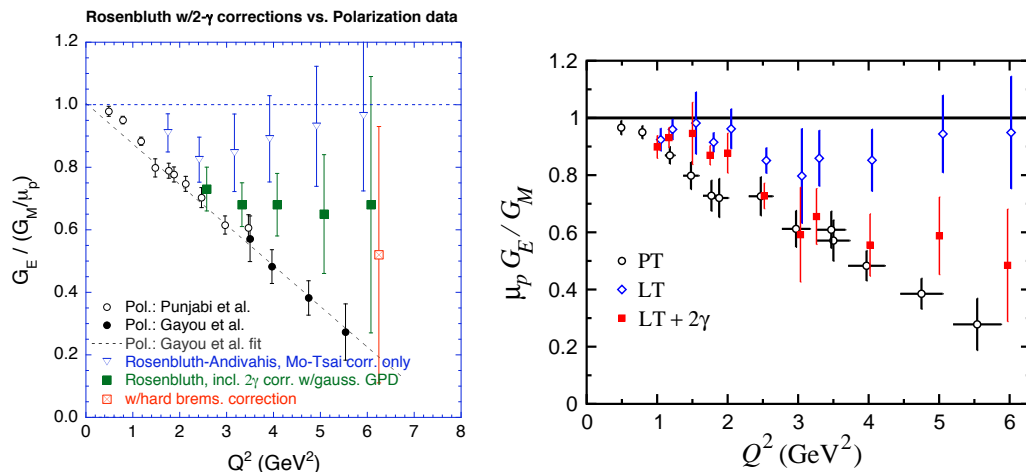


Fig. 5. Determinations of the proton  $G_E/G_M$  ratio with  $2\gamma$  corrections calculated within the partonic framework (left panel) [22,23] or using a single proton as the hadronic intermediate state (right panel) [25]. Left panel : polarization data from [5,6], Rosenbluth data from [24], which include only the well-known Mo-Tsai corrections. The Rosenbluth  $G_E/G_M$  include the  $2\gamma$  corrections, and for one point also a hard bremsstrahlung correction, still using Andivahis *et al.* data. Right panel : “PT” is  $G_E/G_M$  obtained from the polarization transfer experiments; “LT” is  $G_E/G_M$  obtained from a Rosenbluth experiment using only the (Mo-Tsai) radiative corrections, and “LT+ $2\gamma$ ” includes the extra  $2\gamma$  corrections.

very likely that hard two-photon exchange corrections are the main culprit in the difference between both experimental techniques [20]. Despite the long history of two-photon exchange corrections, see Ref. [21] for a review, it is interesting to note that concepts developed over the past decade, such as generalized parton distributions which describe two-photon processes with one or two large photon virtualities, enter when quantifying two-photon exchange corrections at larger  $Q^2$ . The model-independent finding is that the hard two-photon corrections hardly affect polarization transfer results, but they do correct the slope of the Rosenbluth plots at larger  $Q^2$  in an important way, towards reconciling both experimental techniques.

As an example, we show in Fig. 5 (left panel) the  $2\gamma$  exchange correction on the extracted  $G_{Ep}/G_{Mp}$  vs.  $Q^2$  within a partonic framework [22,23]. One set of data points, falling linearly with  $Q^2$ , is from the polarization experiments. Another set of data points, roughly constant in  $Q^2$  and plotted with inverted triangles, is from Rosenbluth data analyzed using only radiative corrections. The solid squares show the best fit  $G_E/G_M$  from [24] data when analyzed including the hard  $2\gamma$  corrections. One sees that for  $Q^2$  in the 2–3 GeV<sup>2</sup> range, the  $G_{Ep}/G_{Mp}$  extracted using the Rosenbluth method including the  $2\gamma$  corrections agree well with the polarization transfer results. At higher  $Q^2$ , there is at least partial reconciliation between the two methods. The effect, in a calculation with just a proton intermediate state, see e.g. [25], is qualitatively similar and shown on the right panel in Fig. 5. Several forthcoming high-precision electron scattering experiments aim at a precision test of these two-photon exchange effects.

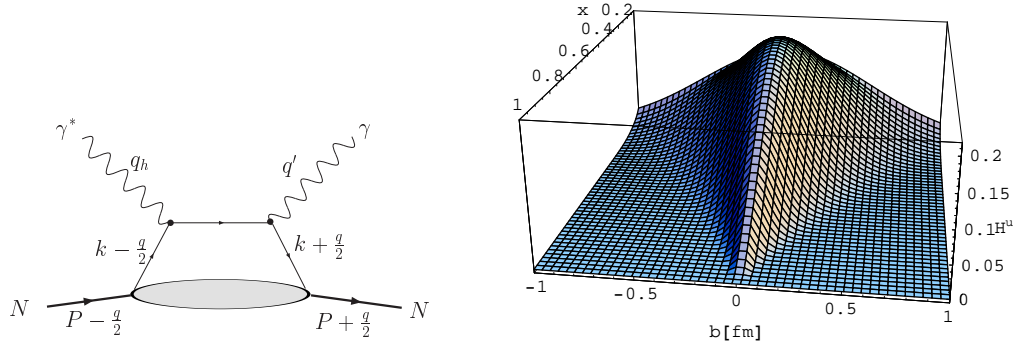


Fig. 6. Left panel : “handbag” diagram for the nucleon DVCS process. Provided the virtuality of the initial photon (with momentum  $q_h$ ) is sufficiently large, the QCD factorization theorem allows to express the total amplitude as the convolution of a Compton process at the quark level and a non-perturbative amplitude parameterized in terms of GPDs (lower blob). Right panel : the GPD  $H^u$  for a valence up-quark in the proton as function of the quark momentum fraction  $x$  and the quark position  $b$  in the transverse plane (perpendicular to the average direction of the fast moving nucleons). The calculation is based on the 3-parameter modified Regge parametrization of [31].

## 2. Generalized Parton Distributions

The nucleon e.m. FFs discussed above access the quark-gluon structure of the nucleon by measuring the matrix element of a well-defined quark-gluon operator (in this case the vector operator  $\bar{q}\gamma^\mu q$ ) over the hadronic state. One is however not limited in nature to probes such as photons (or  $W$ ,  $Z$  bosons for the axial transition). The phenomenon of asymptotic freedom of QCD, meaning that at short distances the interactions between quarks and gluons become weak, provides us with more sophisticated QCD operators to explore the structure of hadrons. Such operators can be accessed by selecting a small size configuration of quarks and gluons, provided by a hard reaction, such as deep inelastic scattering (DIS), or hard exclusive reactions such as deeply virtual Compton scattering (DVCS),  $\gamma^*(q_h) + N(p) \rightarrow \gamma(q') + N(p')$ , where the virtual photon momentum  $q_h$  is the hard scale, see left panel of Fig. 6. The common important feature of such hard reactions is the possibility to separate clearly the perturbative and nonperturbative stages of the interactions : this is the so-called factorization property. The non-perturbative stage of such hard exclusive electroproduction processes is described by universal objects, so-called generalized parton distributions (GPDs), see [26,27,28,29,30] for reviews and references.

The nucleon structure information entering the nucleon DVCS process, can be parameterized at leading twist-2 level, in terms of four (quark chirality conserving) GPDs, depending on three variables: the quark longitudinal momentum fractions  $(x + \xi)$  of initial quark,  $(x - \xi)$  of final quark, and the momentum transfer  $Q^2 = -q^2$  to the nucleon. The interplay between the  $x$  and  $Q^2$ -dependence of the GPDs contains new nucleon structure information beyond the information encoded in forward parton distributions depending only on  $x$ , or FFs depending only on  $Q^2$ . A Fourier transform of the  $Q^2$ -dependence of GPDs accesses the distributions of parton in the transverse plane [13]. For the vector GPD  $H^q$  at  $\xi = 0$ , this Fourier integral in transverse momentum  $q_\perp$  reads as:

$$H^q(x, \mathbf{b}_\perp) \equiv \int \frac{d^2 \mathbf{q}_\perp}{(2\pi)^2} e^{i\mathbf{b}_\perp \cdot \mathbf{q}_\perp} H^q(x, \xi = 0, -\mathbf{q}_\perp^2), \quad (2)$$

and an analogous definition for the other GPDs. These impact parameter GPDs have the physical meaning of measuring the probability to find a quark which carries longitudinal momentum fraction  $x$  at a transverse position  $\mathbf{b}_\perp$  (relative to the transverse center-of-momentum) in a nucleon, see [13]. The right panel of Fig. 6 shows the GPD  $H^u$ , for an  $u$ -quark, within a 3-parameter modified Regge GPD parameterization [31].

Besides providing a tomographic view of the nucleon, GPDs also allow an access to the angular momentum of quark ( and gluons ) in the nucleon [32], for a comparison with recent lattice calculations see [16].

On the experimental side, the first round of experiments dedicated to measure hard exclusive processes such as deeply virtual Compton scattering have been completed at HERMES, HERA, and JLab@6GeV, indicating the dominance of the twist-2 mechanism. For a discussion of some of these results, see [33]. Furthermore, accessing the nucleon GPDs is a major project for the planned JLab 12 GeV upgrade.

### 3. Nucleon excitation spectrum

The understanding of the nucleon excitation spectrum is tightly linked to its structure. The first baryon excited state, the  $\Delta(1232)$  resonance has been charted in particular detail in recent years, see [34] for a recent review and references. At low  $Q^2$ , the measurement of  $\gamma N \Delta$  FFs have allowed to unambiguously map out the small  $E2$  and  $C2$  amplitudes revealing  $d$ -wave components in the nucleon and / or  $\Delta$  wave functions. In parallel, recent years have also seen the development of a chiral effective field theory ( $\chi$ EFT) with two distinct light mass scales : the pion mass and the  $\Delta - N$  mass difference [35,36,37,38].

In Fig. 7 we show the next-to-leading order (NLO)  $\chi$ EFT results for the  $Q^2$  dependence of the  $\gamma N \Delta$  resonant multipoles, at the resonance position, characterized by magnetic dipole ( $M1$ ), electric quadrupole ( $E2$ ) and Coulomb quadrupole ( $C2$ ) transitions. The red solid curve is *with* and the green dotted curve *without* the chiral-loop corrections. We observe from the figure that the chiral loops play a crucial role in the low momentum-transfer dependence of the  $E2/M1$  ( $R_{EM}$ ) ratio. The effect of the “pion cloud” is most pronounced in the  $E2$   $\gamma N \Delta$  transition.

Such  $\chi$ EFT was found to be useful in a dual way : both to describe observables and as a tool to extrapolate lattice results. The latter is demonstrated on the right panel of Fig. 7 which shows the  $m_\pi$ -dependence of the ratios  $R_{EM}$  and  $R_{SM}$  within the  $\chi$ EFT framework in comparison with the lattice QCD calculations. It is seen in particular that the opening of the decay channel due to  $\Delta \rightarrow \pi N$  decay, at  $m_\pi = M_\Delta - M_N$ , leads to strong non-analytic behavior in quark mass. For lattice studies, the  $\Delta(1232)$  resonance, as a purely elastic resonance, is an ideal test case to study the issues, due to opening of decay channels, which are relevant for the whole baryonic spectrum.

### 4. Conclusions

The recent round of double polarization measurements in elastic  $eN$  scattering have led to precise extractions of nucleon e.m. FFs. At low  $Q^2$  values, they allow to test the

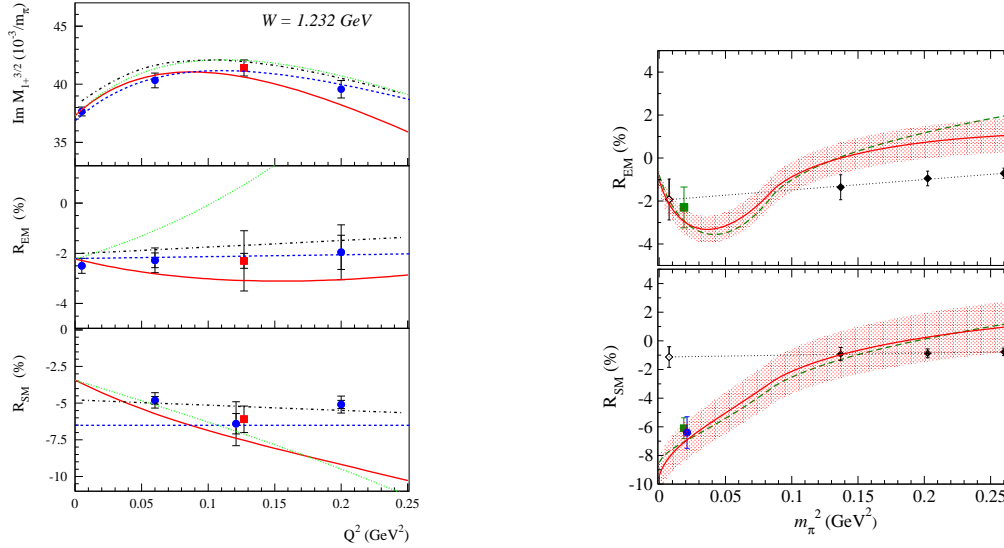


Fig. 7. Left panel : resonant multipoles of pion electroproduction as function  $Q^2$  at the  $\Delta$ -resonance position. Dotted curves :  $\Delta$ -contribution alone. Solid curves : results of the NLO calculation of [38]. Also shown are results of the SAID analysis (FA04K) [40] (dashed-dotted curves), and the MAID 2003 analysis [39] (dashed curves). The data points are from BATES (red solid square) and MAMI (blue solid circles), for references see [34]. Right panel : pion mass dependence of  $E2/M1$  ( $R_{EM}$ ) (upper panel) and  $C2/M1$  ( $R_{SM}$ ) (lower panel), at  $Q^2 = 0.1 \text{ GeV}^2$ . Data points from MAMI (blue circle) and BATES (green squares). The three filled black diamonds at larger  $m_\pi$  are lattice calculations [41], whereas the open diamond near  $m_\pi \simeq 0$  represents their extrapolation assuming linear dependence in  $m_\pi^2$ . The red solid curves are the NLO result of [38], and the error bands are an estimate of the theoretical uncertainty.

pion cloud of the nucleon. At  $Q^2$  values of several  $\text{GeV}^2$ , the difference between the new polarization data and the unpolarized Rosenbluth data is now mainly understood as being due to two-photon exchange effects which largely contribute to the Rosenbluth data in contrast to the polarization transfer results. The precise new data base for the nucleon e.m. FFs allows to map out the transverse quark densities in a fast moving nucleon. On the theoretical side, the state-of-the-art in ab initio calculations of nucleon e.m. FFs from lattice QCD is that unquenched calculations are now feasible for the isovector nucleon e.m. FFs. They are performed for pion masses down to about  $m_\pi \simeq 350 \text{ MeV}$ , into the regime where chiral effects are important. Although the lattice isovector FFs show clear tendency to approach their experimental values as the pion mass decreases to its physical value, the precision of the FF data clearly calls for lattice calculations closer to the chiral limit. Besides, for a calculation of isoscalar FFs, allowing the separate predictions of proton and neutron e.m. FFs, the evaluation of disconnected diagrams is a high priority.

GPDs have emerged over the past decade as a unifying theme in hadron physics linking the spatial densities extracted from FFs with the quark momentum distribution information residing in quark structure functions. They also allow an access to the angular momentum carried by quarks ( and gluons ) in the nucleon. The first round of experiments dedicated to measure hard exclusive processes indicate the dominance of

the twist-2 mechanism at available momentum transfers. Future programs at Compass and a uniquely dedicated program at JLab@12GeV will provide a wide survey of such distributions.

The recent results on the e.m. excitation of the  $\Delta(1232)$  resonance, have also briefly been reviewed. Recently developed chiral effective field theories have emerged which can be useful both to describe observables and as a tool to extrapolate lattice QCD results.

## References

- [1] C. E. Hyde-Wright and K. de Jager, *Ann. Rev. Nucl. Part. Sci.* **54**, 217 (2004).
- [2] J. Arrington, C. D. Roberts and J. M. Zanotti, *J. Phys. G* **34**, S23 (2007).
- [3] C. F. Perdrisat, V. Punjabi and M. Vanderhaeghen, *Prog. Part. Nucl. Phys.* **59**, 694 (2007).
- [4] M. K. Jones *et al.* [Jefferson Lab Hall A Collaboration], *Phys. Rev. Lett.* **84**, 1398 (2000).
- [5] O. Gayou *et al.* [JLab Hall A Coll.], *Phys. Rev. Lett.* **88**, 092301 (2002).
- [6] V. Punjabi *et al.*, *Phys. Rev. C* **71**, 055202 (2005) [Erratum-ibid. *C* **71**, 069902 (2005)].
- [7] J. Arrington, *Phys. Rev. C* **68**, 034325 (2003).
- [8] J. J. Kelly, *Phys. Rev. C* **70**, 068202 (2004).
- [9] M. Kohl, these proceedings.
- [10] J. Friedrich and T. Walcher, *Eur. Phys. J. A* **17**, 607 (2003).
- [11] G. A. Miller, *Phys. Rev. Lett.* **99**, 112001 (2007).
- [12] C. E. Carlson and M. Vanderhaeghen, arXiv:0710.0835 [hep-ph].
- [13] M. Burkardt, *Phys. Rev. D* **62**, 071503 (2000); *Int. J. Mod. Phys. A* **18**, 173 (2003).
- [14] J. Arrington, W. Melnitchouk and J. A. Tjon, arXiv:0707.1861 [nucl-ex].
- [15] R. Bradford, A. Bodek, H. Budd and J. Arrington, *Nucl. Phys. Proc. Suppl.* **159**, 127 (2006).
- [16] A. Schäfer, these proceedings.
- [17] R. G. Edwards *et al.*, *PoS LAT2006*, 121 (2006).
- [18] S. Ohta, these proceedings.
- [19] G. V. Dunne, A. W. Thomas and S. V. Wright, *Phys. Lett. B* **531**, 77 (2002).
- [20] P. A. M. Guichon and M. Vanderhaeghen, *Phys. Rev. Lett.* **91**, 142303 (2003).
- [21] C. E. Carlson and M. Vanderhaeghen, *Ann. Rev. Nucl. Part. Sci.* **57**, 171 (2007).
- [22] Y. C. Chen, A. Afanasev, S. J. Brodsky, C. E. Carlson and M. Vanderhaeghen, *Phys. Rev. Lett.* **93**, 122301 (2004).
- [23] A. V. Afanasev, S. J. Brodsky, C. E. Carlson, Y. C. Chen and M. Vanderhaeghen, *Phys. Rev. D* **72**, 013008 (2005).
- [24] L. Andivahis *et al.*, *Phys. Rev. D* **50**, 5491 (1994);
- [25] P. G. Blunden, W. Melnitchouk and J. A. Tjon, *Phys. Rev. Lett.* **91**, 142304 (2003); *Phys. Rev. C* **72**, 034612 (2005).
- [26] X. D. Ji, *J. Phys. G* **24**, 1181 (1998).
- [27] K. Goeke, M. V. Polyakov and M. Vanderhaeghen, *Prog. Part. Nucl. Phys.* **47**, 401 (2001).
- [28] M. Diehl, *Phys. Rept.* **388**, 41 (2003).
- [29] X. Ji, *Ann. Rev. Nucl. Part. Sci.* **54**, 413 (2004).
- [30] A. V. Belitsky and A. V. Radyushkin, *Phys. Rept.* **418**, 1 (2005).
- [31] M. Guidal, M. V. Polyakov, A. V. Radyushkin and M. Vanderhaeghen, *Phys. Rev. D* **72**, 054013 (2005).
- [32] X. D. Ji, *Phys. Rev. Lett.* **78**, 610 (1997);
- [33] P. Y. Bertin, these proceedings.
- [34] V. Pascalutsa, M. Vanderhaeghen and S. N. Yang, *Phys. Rept.* **437**, 125 (2007).
- [35] E. Jenkins and A. V. Manohar, *Phys. Lett. B* **255**, 558 (1991).
- [36] T. Hemmert, B. R. Holstein and J. Kambor, *Phys. Lett. B* **395**, 89 (1997); *J. Phys. G* **24**, 1831 (1998).
- [37] V. Pascalutsa and D. R. Phillips, *Phys. Rev. C* **67**, 055202 (2003).

- [38] V. Pascalutsa and M. Vanderhaeghen, Phys. Rev. Lett. **95**, 232001 (2005); Phys. Rev. D **73**, 034003 (2006).
- [39] D. Drechsel, O. Hanstein, S. S. Kamalov and L. Tiator, Nucl. Phys. A **645**, 145 (1999).
- [40] R. A. Arndt, W. J. Briscoe, I. I. Strakovsky and R. L. Workman, Phys. Rev. C **66**, 055213 (2002).
- [41] C. Alexandrou, P. de Forcrand, H. Neff, J. W. Negele, W. Schroers and A. Tsapalis, Phys. Rev. Lett. **94**, 021601 (2005).